CHIN. PHYS. LETT. Vol. 38, No. 6 (2021) 068202

# $LiCoO_2$ Epitaxial Film Enabling Precise Analysis of Interfacial Degradations

Changdong Qin(秦昌东)[1], Le Wang(王乐)[2], Pengfei Yan(闫鹏飞)[1*], Yingge Du(杜英歌)[2*], and Manling Sui(隋曼龄)[1*]

[1]*Beijing Key Laboratory of Microstructure and Property of Solids, Faculty of Materials and Manufacturing, Beijing University of Technology, Beijing 100124, China*

[2]*Physical and Computational Sciences Directorate, Pacific Northwest National Laboratory Richland, WA 99354, USA*

(Received 9 February 2021; accepted 2 April 2021; published online 25 May 2021)

Interfacial structure evolution and degradation are critical to the electrochemical performance of $LiCoO_2$ (LCO), the most widely studied and used cathode material in lithium ion batteries. To understand such processes requires precise and quantitative measurements. Herein, we use well-defined epitaxial LCO thin films to reveal the interfacial degradation mechanisms. Through our systematical investigations, we find that surface corrosion is significant after forming the surface phase transition layer, and the cathode electrolyte interphase (CEI) has a double layer structure, an inorganic inner layer containing CoO, LiF, $LiOH/Li_2O$ and $Li_xPF_yO_z$, and an outmost layer containing $Li_2CO_3$ and organic carbonaceous components. Furthermore, surface cracks are found to be pronounced due to mechanical failures and chemical etching. This work demonstrates a model material to realize the precise measurements of LCO interfacial degradations, which deepens our understanding on the interfacial degradation mechanisms.

DOI: 10.1088/0256-307X/38/6/068202

As the first generation of layered lithium transition metal oxides, $LiCoO_2$ (LCO) is a high power and high energy density cathode for lithium ion batteries (LIBs).[1,2] After being commercialized for several decades, its energy storage potential is still under exploration. For instance, efforts on improving LCO's high voltage cycling stability have gained extensive attention.[3–5] High cycling voltage imposes the LCO material into harsh chemical and mechanical conditions, leading to aggravated degradations both at the surface and in the bulk. At the surface, high voltage cycling leads to severe side reactions, exacerbating surface corrosion,[6,7] thickening the surface phase transformation layer (PTL) and the cathode/electrolyte interphase layer (CEI).[8–11] In the bulk material, deep delithiation can trigger phase transitions, causing irreversible structure changes[8,12,13] and mechanical cracking.[14,15]

Cathode/electrolyte interfacial degradations are crucial to the electrochemical performance, thus various characterization methods and techniques have been devoted to understanding the degradation mechanisms.[16–20] For the surface PTL, it is featured with the changes of lattice structure and chemical composition. Different from traditional NMC layered cathodes, which usually develop a rock salt structured layer,[21,22] the $LiCoO_2$ layered cathodes tend to form a spinel-like structure at the surface.[12,23,24] For the CEI, it contains both organic and inorganic components, whose chemical composition is similar to anode/electrolyte interphase (AEI) at the anode material.[10,25,26] It was argued that it is AEI at the anode surface that is transferred through the electrolyte and deposited onto the cathode surface during electrochemical cycling.[10,27] By virtue of *in situ* techniques, it was found that the CEI layer gradually accumulates with cycle numbers.[28] It was also reported that the CEI layer was formed at high voltage and disappeared at low voltage.[9] For the conventional LCO electrode, CEI is usually composed of LCO particles, conductive additive, and organic binder. Therefore, it is difficult to obtain the exact composition of CEI layers. As for the LCO particles, the exact thickness of surface phase transition layer as well as the corrosion rate is technically hard to quantify. Additive-free epitaxial thin films provide advantages over powders in fundamental interfacial studies.[29,30] The defect evolution and the thickness changes of the CEI layer upon cycling have been studied.[31–33] Moreover, using epitaxial film can realize quantitative and precise measurements of interfacial degradations because of the well-defined pristine state.

Supported by the National Natural Science Fund for Innovative Research Groups (China) (Grant No. 51621003), the National Key Research and Development Program of China (Grant No. 2016Yu7FB0700700), the Beijing Municipal Fund for Scientific Innovation (Grant No. PXM2019_014204_500031) and the Beijing Municipal High Level Innovative Team Building Program (Grant No. IDHT20190503). The film growth is supported by the U.S. Department of Energy (DOE), Office of Science, Office of Basic Energy Science, Early Career Research Program under Award #68272, and performed using EMSL (grid.436923.9), a DOE Office of the Science User Facility sponsored by the Biological and Environmental Research Program.

*Corresponding authors. Email: pfyan@bjut.edu.cn; yingge.du@pnnl.gov; mlsui@bjut.edu.cn

© 2021 Chinese Physical Society and IOP Publishing Ltd

In this work, we use additive-free, epitaxial LCO films to conduct in-depth investigation on the interfacial degradation mechanisms by virtue of XPS and scanning transmission electron microscopy (STEM) with energy dispersive spectroscopy (EDS). The use of epitaxial LCO films enables us to directly and quantitatively measure the (104) facet surface corrosion upon electrochemical cycling. Combining chemical analysis, we provide a more accurate model for the CEI layer in terms of both morphology and chemical composition. Moreover, the surface crack is also found to be a serious degradation. We demonstrate that using the epitaxial LCO film can more precisely characterize the LCO interfacial degradations.

*Experiment—Materials and Electrochemical Tests.* LCO thin films were grown on (001)-oriented Nb-doped $SrTiO_3$ (STO) substrates by pulsed laser deposition (PLD) at a substrate temperature of about 600 ℃ and $O_2$ pressure of about 10 mTorr. Details were described elsewhere.[34] $LiCoO_2$ powders were purchased from Shenzhen Kejing Star Technology Co., Ltd. Both LCO films and particles are assembled into CR2032 coin cells for the electrochemical test. For the LCO-film cells, we replace the conventional LCO cathode foils with the LCO/STO chips, where the Nb-doped STO substrate is acting as the current collector. The STO substrate was coated with Au to improve the electronic conductivity. All the cells are assembled in an Ar-filled glove box. The liquid electrolyte used in this work was 1 M $LiPF_6$ dissolved in ethylene carbonate (EC) and dimethyl carbonate (DMC) (1:1). Polypropylene (Celgard 2400) and Li metal were used as the separator and anode, respectively. Galvanostatic charge/discharge tests of the cells were performed using a CT4000 cell test instrument from Neware Co., Ltd.

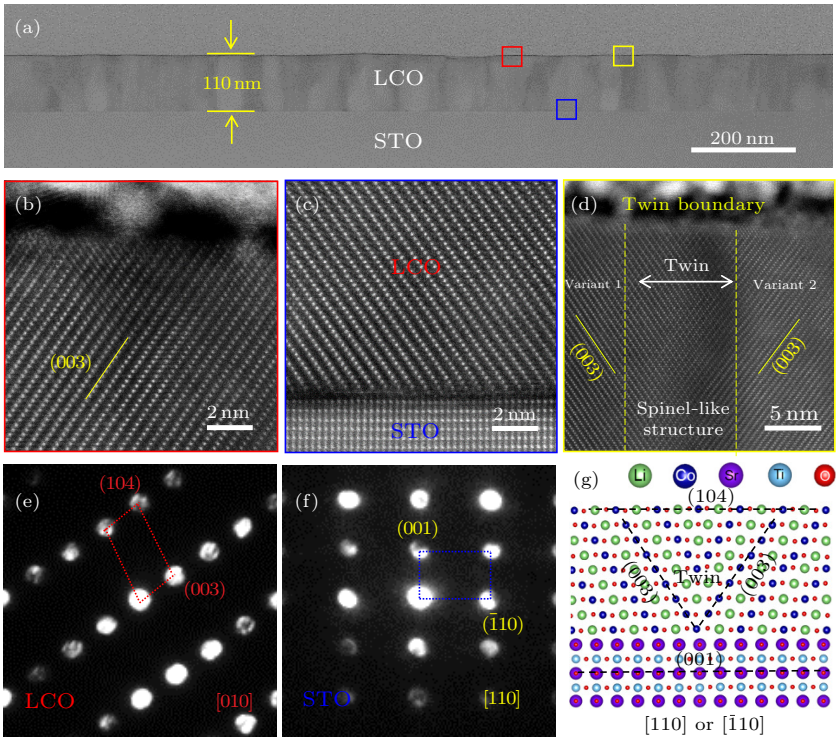


**Fig. 1.** (a) STEM-HAADF image of the cross section showing the uniform epitaxial LCO film. Atomic resolution STEM-HAADF images (b) at the pristine LCO surface and (c) at the LCO/STO interface from the red and blue regions in (a). (d) STEM-HAADF image of a twin boundary of two neighbored variants [from the yellow frame in (a)], where the twin boundary region is highly mixed and appears as the spinel-like structure. NBD patterns from LCO (e) and STO (f), respectively. (g) The structure model of the LCO/STO interface to show the epitaxial relationship and the variants geometry from two equivalent axes [110] and [$\bar{1}$10].

*Characterization.* The cross-sectional samples prepared for TEM characterizations were conducted on an FEI Helios NanoLab 600i focused ion beam (FIB) operated at 2–30 kV. To protect the surface layer from beam damage and contamination, the 1.5-μm-thick Pt layer was deposited on a particle surface to void the Ga ion-beam damage in the subsequent lift-out and thinning process. All the specimens were thinned to less than 200 nm. STEM-HAADF imaging, spatially resolved EDS, nano-beam diffraction (NBD) were performed on a 300 kV Titan G2 60–300 microscope equipped with a probe spherical aberration corrector and "super X" EDS system. Esprit 1.9 software was used to quantify the EDS data. The equipment of ESCALAB 250 Xi with monochromatic 150 W Al $K_\alpha$ radiation provided by Thermo Fisher was used to detect the x-ray photoelectron spectroscopy (XPS) signal. In order to minimize the effects of oxygen and

moisture in air, cells were disassembled and washed in DMC carefully in an Ar-filled glove box. All samples were protected from air by Ar-filled aluminum foil bags before being moved to the detector cavity. The data was analyzed with program XPS Peak and the binding energies were referenced to the C 1*s* line at 284.5 eV from adventitious carbon.

*Results and Discussion—Pristine Epitaxial Film.* Our microanalysis in Fig. 1(a) reveals that the pristine LCO film is uniform with a thickness of ∼110 nm. EDS maps in Fig. S1 of the Supporting Information clearly show the homogenous element distribution over the entire film. The pristine LCO epitaxial film shows the well-defined layered structure as verified by STEM-HAADF images. Figures 1(b) and 1(c) show the lattice structure at the surface layer and the interface region, respectively. Based on our observations, the Li-containing channels, i.e., the LCO (003) planes as shown in Figs. 1(b)–1(d), can display two different orientations with respect to the STO substrate. These two different orientated variants are in a twin relationship to each other as shown in Fig. 1(d). The twin boundary is not sharp. There is strong interlayer mixing and overlapping effect, as shown in Fig. 1(d). The nano beam diffraction (NBD) patterns [Figs. 1(e) and 1(f)] from the LCO film and the STO substrate further identified the epitaxial geometry, in which the (104) planes are always parallel to the STO (001) planes. Since the [100] is equal to [010] for the STO substrate, the as-grown LCO films actually contain four equivalent variants as determined by the four-fold symmetry of the STO (001) substrate. Figure 1(g) shows the two equivalent variants either from [110] or [$\bar{1}$10] axis. Neighbored variants are in a twin relationship. Thus, many twin boundaries exist in the epitaxial film. In addition, we also observed some $Co_3O_4$ impurity inside the film as shown in Fig. S2, even though the overall layered structure is confirmed by out-of-plane XRD as shown in Fig. S3 of the Supporting Information.

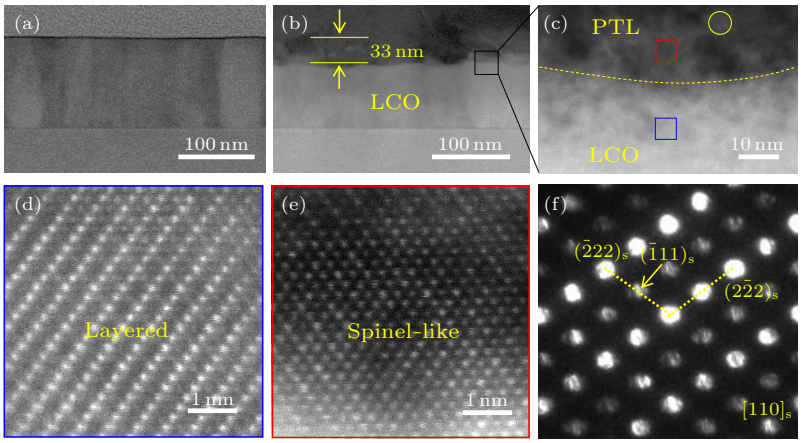


**Fig. 2.** STEM-HAADF image of cross section showing (a) the pristine LCO film grown on STO(001) and (b) after 50 cycles at 2.7–4.5 V. (c) STEM-HAADF image at the LCO/PTL interface from the black region in (b). (d)–(e) Atomic resolution STEM-HAADF image from blue and red region in (c). (f) NBD pattern from the yellow area in (c). Subscript S represents the "spinel structure" to denote the phase of PTL.

*Surface Degradation and Corrosion.* The LCO film is cycled at voltage window 2.7–4.5 V for 50 cycles (Fig. S4). In order to improve the electronic conductivity, we deposited an Au layer on the epitaxial sample. Figure S4 shows the electrochemical performance of the sample with/without the Au coating layer. Although the capacity is still lower than that of conventional LCO particle electrodes, the LCO degradation mechanisms are universal, which guarantees our study on the interfacial degradations is useful. After cycling, the film develops a thick PTL and CEI layer at the surface, which is similar to the LCO particles. As shown in Fig. 2(a), the pristine LCO film has a uniform thickness (∼110 nm) and atomic flat surface. In contrast, Fig. 2(b) shows the LCO film after 50 cycles, where the surface is not flat and the thickness is decreased (marked by the yellow arrows). Figure 2(c) shows the enlarged surface region in Fig. 2(b), where many pores (black dots) are developed due to severe surface corrosion effect. Noticing the film thickness difference between Fig. 2(a) and Fig. 2(b), we can see that the LCO surface corrosion is significant during battery cycling, which is ∼33 nm after 50 cycles. Corrosion-induced thickness change varies at different sites (from 15 nm to 33 nm, shown in Fig. S5), but direct evidence and quantitative results on the surface corrosion effect are shown, which cannot be estimated precisely using conventional LCO particles. On the other hand, we find that the thickness of the phase transition layer (PTL) at different sites is nearly the same, which is about 35 nm (Fig. S5) after 50 cycles at 2.7–4.5 V cycling. Thus, in our case, both the PTL and corrosion layer can be quantitatively identified, which has not been revealed before.[31,32] Our results demonstrate that the surface corrosion can be as fast as 0.7 nm per cycle, which is a drastic chemical reac-

tion. Surface corrosion induced loss of active material as well as the Co dissolution into the electrolyte can significantly affect the cycling performance.[6,8,35] As shown in Figs. 2(d) and 2(e), interlayer mixing gradually increases from bulk to surface. The severely corroded surface layer is in a spinel-like structure as evidenced by Figs. 2(e) and 2(f). According to our recent work, the PTL featured with porous morphology and a spinel-like structure has minor blocking effects on Li ion diffusion.[36] However, forming the PTL is accompanied by Co dissolution, oxygen loss and Li depletion, which will definitely facilitate the corrosion process.

*CEI Characteristics.* Above the PTL, a thick CEI layer is also developed on the surface, as verified by the SEM images in Fig. S6. For an in-depth understanding of the structure and components distribution of CEI, we further conducted detailed characterization on the CEI region by virtue of STEM-HAADF and EDS. As the low magnification images shown in Figs. 3(a) and 3(b), the CEI has a double-layer structure: a subsurface layer consisting of mosaics and an outmost uniform layer, which has been highlighted by the yellow lines. The mosaic layer appeared as polycrystalline features. Further selected area electron diffraction (SAED) confirms that it contains many CoO crystallites. As shown in Fig. 3(c), the SAED pattern [taken from the circled area in Fig. 3(b)] can be assigned as polycrystalline CoO. Zooming in the red area in Fig. 3(b), we can see many nano-sized crystals with an average size of ∼4 nm as shown in Fig. 3(d). A high-resolution STEM-HAADF image further proves that the bright contrast nanocrystals are CoO particles [Fig. 3(e)], which has been shown to form as a result of over-delithiation.[34] Overall, EDS mapping [Fig. 3(f) and Fig. S7] reveals that the outermost layer of CEI is mainly composed of carbonaceous substances and the mosaic subsurface layers are made up of CoO particles and other inorganic substances containing oxygen, fluorine, and phosphorus.

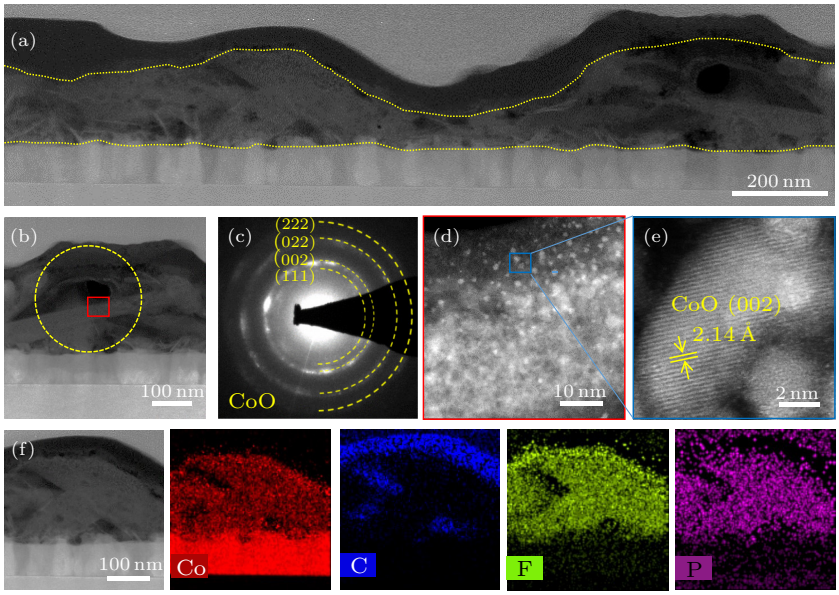


**Fig. 3.** [(a), (b)] Low magnification STEM-HAADF images of LCO film after 50 cycles at 2.7–4.5 V. (c) SAED pattern of the CEI layer from the area marked with a yellow circle in (b). (d) High magnification STEM-HAADF of mosaic from the red area in (b). (e) High-resolution STEM-HAADF image of CoO particles from the blue area in (d). (f) STEM-EDS mapping of the CEI layer.

To further characterize the CEI composition and its evolution upon electrochemical cycling, XPS was conducted on the additive-free LCO film. The O 1*s*, F 1*s* and Co 2*p* photoemission spectra are measured. We compare the pristine film and the cycled film at a fully discharged state. Figure 4 shows the XPS evolution upon cycling. In order to interpret the evolution of each component properly, their XPS signals are listed in Table 1. Figure 4(a) show the O 1*s* signals, in which we can see lattice oxygen signal decreases significantly after 30 cycles and then disappears after 50 cycles, indicating the continuous growth of the CEI layer upon cycling. Increasing cycle numbers leads to C=O/$Li_2CO_3$ and LiOH/$Li_2O$ signals continuously increase. While the C–O peak from $ROCO_2Li$, $OP(OR)_3$, (R representing $CH_2$ or $CH_3$ groups) and polycarbonate-type compounds does not increase, which is different from the previous results from conventional LCO electrode foil, indicating that C–O species are not the main component of CEI. Figure 4(b) shows the F 1*s* spectra. Two major peaks appear after cycle at 685.6 eV and 687.3 eV representing LiF and $Li_xPF_yO_z$, respectively, which are attributed to the decomposition of Li salt. The Li 1*s* and C 1*s* spectra in Fig. S8 also indicate that the peak intensity of $Li_2CO_3$, LiF and $Li_xPF_yO_z$ increase pronounced af-

ter cycling. Based on the XPS spectra, it can be concluded that $Li_2CO_3$, $LiOH/Li_2O$, LiF and $Li_xPF_yO_z$ are the main components of CEI. Figure 4(c) shows the Co 2*p* spectra, in which we can clearly see the reduction of Co upon cycling. The changes of energy distance $\Delta E_{m,s}$ between the main photoelectron peak and satellite S peak can show the valence states of Co. $\Delta E_{m,s}$ is about 6 eV for divalent transition metal ions ($Co^{2+}$) and increases to 9–11 eV for tri- and tetra-valent cations ($Co^{3+}/Co^{4+}$).[27,37] In our case, the $\Delta E_{m,s}$ decreases from 9.9 eV to 6.2 eV and satellite intensity increases significantly, indicating the divalent $Co^{2+}$ in the CEI layer. The results match well with our previous TEM observations (Fig. 3). After 50 cycles, Co 2*p* signal is below the detection level of XPS, indicating the formation of a thick carbon-containing top CEI layer (XPS is sensitive to the top 5–10 nm). Therefore, combining previous EDS measurements, the components of CEI are CoO, LiF, $Li_xPF_yO_z$ and $LiOH/Li_2O$, and the outmost layer is composed of $Li_2CO_3$ and other organic carbonaceous products from electrolyte decomposition.

**Table 1.** Components corresponding to each XPS peak.

| | Binding energy (eV) | Components |
|---|---|---|
| O 1*s* | ~529.7 eV | Lattice oxygen in $LiCoO_2$ |
| | ~531.0 eV | $LiOH/Li_2O$ |
| | ~532.0 eV | $Li_2CO_3$ or O–C=O |
| | ~533.5 eV | O–C in O–C=O or $OP(OR)_3$ |
| F 1*s* | ~685.5 eV | LiF or metal fluorides |
| | ~686.6 eV | $Li_xPF_yO_z$ |

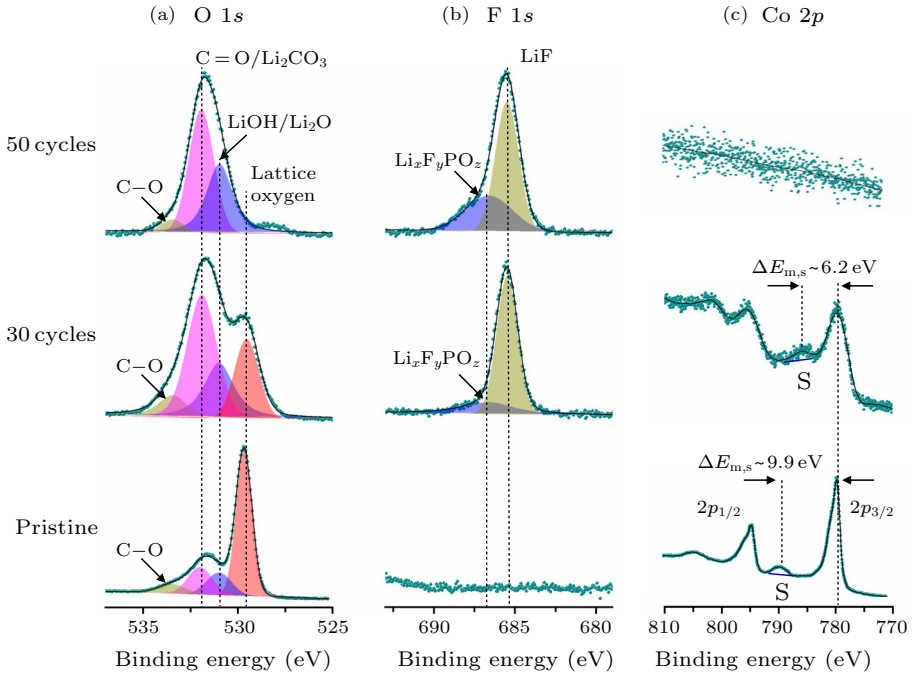


**Fig. 4.** (a) O 1*s*, (b) F 1*s* and (c) Co 2*p* XPS spectra of pristine, 30 cycles and 50 cycles at 2.7–4.5 V from bottom to the top, respectively.

*Surface Cracking.* Cracking is a frequently observed mechanical failure in LCO. From the SEM image, we can clearly observe the high density of surface cracks in cycled LCO particles after 100 cycles at 2.7–4.5 V, as shown in Fig. 5(a) and Fig. S9. It is worth pointing out that cracking always occurs even at different cycling voltages as shown in Fig. S9, while cracking occurs faster and more severe at high voltage cycling as verified by the SEM images. Such surface cracks are also observed in the LCO epitaxial films after the same cycling as shown in Fig. 5(b). In the STEM-HAADF image, more cracks are shown in the cross-sectional view as indicated by the arrows in Fig. 5(c), which reveal that they do not penetrate through the film to the substrate. Besides the vertical cracks (yellow arrows), smaller cracks parallel to the LCO/STO interfaces are also observed as highlighted by the red arrows in Fig. 5(c). By examining the vertical crack region, as shown in Fig. 5(d), we find the PTL is in thickness of ~101 nm, thicker than those previously estimated.[31,36] As evidenced by Figs. 5(e) and 5(f), the structure in PLT is transformed into a spinel-like structure. Phase transition from the layered structure to the spinel structure can cause significant volume change, which is the major driving force of the surface cracking. Cracking leads to the exposure of more fresh surfaces to the electrolyte, which increases electrode/electrolyte side reactions and aggravates dissolution/reduction of transition metal ions and oxygen loss.[15,38,39] As shown in Fig. S10, the EDS mapping images show the accumulation of carbon, fluorine and phosphorus inside the crack.

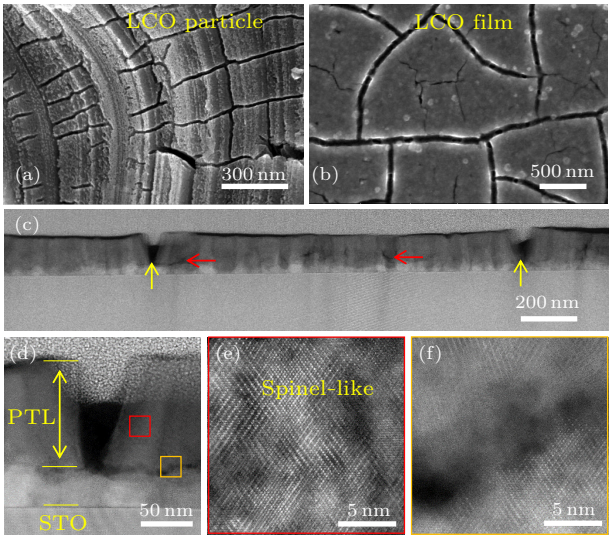


**Fig. 5.** SEM images of (a) an LCO particle and (b) a ∼110 nm LCO film grown on STO (001) cycled at 4.5 V for 100 cycles. [(c), (d)] Cross-sectional STEM-HAADF images of cracks in LCO film after the cycle. [(e), (f)] High-resolution STEM-HAADF images from the red and orange area in (d).

*Effects of Interfacial Degradations.* In this work, we investigate the structural degradation mechanisms and the formation of CEI layers in well-defined LCO epitaxial thin films. Upon electrochemical cycling, the interfacial degradations in LCO can be categorized into three aspects. Firstly, surface layer phase transition and surface corrosion are severe upon electrochemical cycling. Our observations indicate that LCO surface phase transition can aggravate the surface corrosion process. Corrosion-induced Co dissolution and O loss degrade the overall electrochemical performance. Moreover, we quantitatively show that the surface corrosion can reach 0.7 nm per cycle. Secondly, we performed structural and chemical imaging of the CEI layers formed on LCO epitaxial films, which are composed of an inner inorganic layer containing CoO, LiF, LiOH/$Li_2O$ and $Li_xPF_yO_z$, and an outmost layer containing $Li_2CO_3$ and organic carbonaceous components. Understanding the composition and structure of the CEI may further allow us to tune its chemistry to facilitate the charge/ion transportation, mitigating both capacity decay and voltage fading. Thirdly, the surface crack is of high density after prolonged cycling. Cracking generates fresh interfaces to incur more severe interfacial side reactions, which further accelerates the interfacial degradations.

In summary, combined with the STEM-HAADF, EDS and XPS characterization, the interfacial degradation occurring in epitaxial LCO thin films have been systematically investigated. We provide direct evidence of cycling-induced surface corrosion and the quantitative corrosion rate (0.7 nm per cycle at 4.5 V) upon electrochemical cycling. Formation of surface PTL is believed to aggravate surface corrosion. Above the PTL layer, the CEI layer is found to have a double-layer structure with an inner inorganic layer containing CoO, LiF, LiOH/$Li_2O$ and $Li_xPF_yO_z$, and an outer layer containing $Li_2CO_3$ and organic carbonaceous components. Furthermore, due to surface layer phase transition, volume change is substantial and the high density of the surface cracks is developed, which results in more fresh surfaces exposed to the electrolyte and thus more electrode/electrolyte side reactions and corrosion. This work highlights that atomically resolved imaging on precisely synthesized model cathode materials can allow for a deeper, quantitative understanding of the electrochemical degradation process, which is critically needed to mitigate both capacity decay and voltage fading.

## References

[1] Goodenough J B and Kim Y 2010 *Chem. Mater.* **22** 587
[2] Li H, Wang Z, Chen L and Huang X 2009 *Adv. Mater.* **21** 4593
[3] Liu Q, Su X, Lei D, Qin Y, Wen J, Guo F, Wu Y A, Rong Y, Kou R, Xiao X, Aguesse F, Bareño J, Ren Y, Lu W and Li Y 2018 *Nat. Energy* **3** 936
[4] Zhang J N, Li Q, Ouyang C, Yu X, Ge M, Huang X, Hu E, Ma C, Li S, Xiao R, Yang W, Chu Y, Liu Y, Yu H, Yang X Q, Huang X, Chen L and Li H 2019 *Nat. Energy* **4** 594
[5] Wang Y, Zhang Q, Xue Z C, Yang L, Wang J, Meng F, Li Q, Pan H, Zhang J N, Jiang Z, Yang W, Yu X, Gu L and Li H 2020 *Adv. Energy Mater.* **10** 2001413
[6] Amatucci G G, Tarascon J M and Klein L C 1996 *Solid State Ionics* **83** 167
[7] Wang H, Rus E, Sakuraba T, Kikuchi J, Kiya Y and Abruna H D 2014 *Anal. Chem.* **86** 6197
[8] Yano A, Shikano M, Ueda A, Sakaebe H and Ogumi Z 2017 *J. Electrochem. Soc.* **164** A6116
[9] Lu W, Zhang J, Xu J, Wu X and Chen L 2017 *ACS Appl. Mater. Interfaces* **9** 19313
[10] Zhang J N, Li Q, Wang Y, Zheng J, Yu X and Li H 2018 *Energy Storage Mater.* **14** 1
[11] Lu Y C, Mansour A N, Yabuuchi N and Shao-Horn Y 2009 *Chem. Mater.* **21** 4408
[12] Gabrisch H, Yazami R and Fultz B 2004 *J. Electrochem. Soc.* **151** A891
[13] Reimers J N 1992 *J. Electrochem. Soc.* **139** 2091
[14] Kikkawa J, Terada S, Gunji A, Nagai T, Kurashima K and Kimoto K 2015 *J. Phys. Chem. C* **119** 15823
[15] Kikkawa J, Terada S, Gunji A, Haruta M, Nagai T, Kurashima K and Kimoto K 2014 *Appl. Phys. Lett.* **104** 114105
[16] Xu K 2014 *Chem. Rev.* **114** 11503
[17] Choi N S, Han J G, Ha S Y, Park I and Back C K 2015 *RSC Adv.* **5** 2732
[18] Aurbach D, Markovsky B, Salitra G, Markevich E, Talyossef Y, Koltypin M, Nazar L, Ellis B and Kovacheva D 2007 *J. Power Sources* **165** 491
[19] Gauthier M, Carney T J, Grimaud A, Giordano L, Pour N, Chang H H, Fenning D P, Lux S F, Paschos O, Bauer C, Maglia F, Lupart S, Lamp P and Shao-Horn Y 2015 *J. Phys. Chem. Lett.* **6** 4653
[20] Wang J, Ji Y, Appathurai N, Zhou J and Yang Y 2017 *Chem. Commun.* **53** 8581
[21] Jung S K, Gwon H, Hong J, Park K Y, Seo D H, Kim H, Hyun J, Yang W and Kang K 2014 *Adv. Energy Mater.* **4** 1300787
[22] Zhao W, Zheng J, Zou L, Jia H, Liu B, Wang H, Engelhard M H, Wang C, Xu W, Yang Y and Zhang J G 2018 *Adv.*

*Energy Mater.* **8** 1800297
[23] Wang H, Jang Y I I, Huang B, Sadoway D R and Chiang Y M 1999 *J. Electrochem. Soc.* **146** 473
[24] Yan P, Xiao L, Zheng J, Zhou Y, He Y, Zu X, Mao S X, Xiao J, Gao F, Zhang J G and Wang C M 2015 *Chem. Mater.* **27** 975
[25] Peled E, Golodnitsky D and Ardel G 1997 *J. Electrochem. Soc.* **144** L208
[26] Aurbach D, Weissman I and Schechter A 1996 *Langmuir* **12** 3991
[27] Verdier S, El O L, Dedryvère R, Bonhomme F, Biensan P and Gonbeau D 2007 *J. Electrochem. Soc.* **154** A1088
[28] Minato T, Kawaura H, Hirayama M, Taminato S, Suzuki K, Yamada N L, Sugaya H, Yamamoto K, Nakanishi K, Orikasa Y, Tanida H, Kanno R, Arai H, Uchimoto Y and Ogumi Z 2016 *J. Phys. Chem. C* **120** 20082
[29] Xia Q, Sun S, Xu J, Zan F, Yue J, Zhang Q, Gu L and Xia H 2018 *Small* **14** 1804149
[30] Nishio K, Ohnishi T, Akatsuka K and Takada K 2014 *J. Power Sources* **247** 687
[31] Tan H, Takeuchi S, Bharathi K K, Takeuchi I and Bendersky L A 2016 *ACS Appl. Mater. Interfaces* **8** 6727
[32] Yasuhara S, Yasui S, Teranishi T, Chajima K, Yoshikawa Y, Majima Y, Taniyama T and Itoh M 2019 *Nano Lett.* **19** 1688
[33] Takeuchi S, Tan H, Bharathi K K, Stafford G R, Shin J, Yasui S, Takeuchi I and Bendersky L A 2015 *ACS Appl. Mater. Interfaces* **7** 7901
[34] Yang Z, Ong P V, He Y, Wang L, Bowden M E, Xu W, Droubay T C, Wang C, Sushko P V and Du Y 2018 *Small* **14** 1803108
[35] Hirooka M, Sekiya T, Omomo Y, Yamada M, Katayama H, Okumura T, Yamada Y and Ariyoshi K 2019 *Electrochim. Acta* **320** 134596
[36] Qin C, Jiang Y, Yan P and Sui M 2020 *J. Power Sources* **460** 228126
[37] Cherkashinin G, Nikolowski K, Ehrenberg H, Jacke S, Dimesso L and Jaegermann W 2012 *Phys. Chem. Chem. Phys.* **14** 12321
[38] Jiang Y, Yan P, Yu M, Li J, Jiao H, Zhou B and Sui M 2020 *Nano Energy* **78** 105364
[39] Wilson J R, Cronin J S, Barnett S A and Harris S J 2011 *J. Power Sources* **196** 3443

# Supporting Information for "$LiCoO_2$ Epitaxial Film Enabling Precise analysis of Interfacial Degradations"

Changdong Qin(秦昌东)[1], Le Wang(王乐)[2], Pengfei Yan(闫鹏飞)[1]* , Yingge Du(杜英歌)[2]*, and Manling Sui(隋曼龄)[1]*

[1]Beijing Key Laboratory of Microstructure and Property of Solids, Faculty of Materials and Manufacturing, Beijing University of Technology, Beijing 100124, China

[2]Physical and Computational Sciences Directorate, Pacific Northwest National Laboratory Richland, WA 99354, USA

E-mail: pfyan@bjut.edu.cn; mlsui@bjut.edu.cn

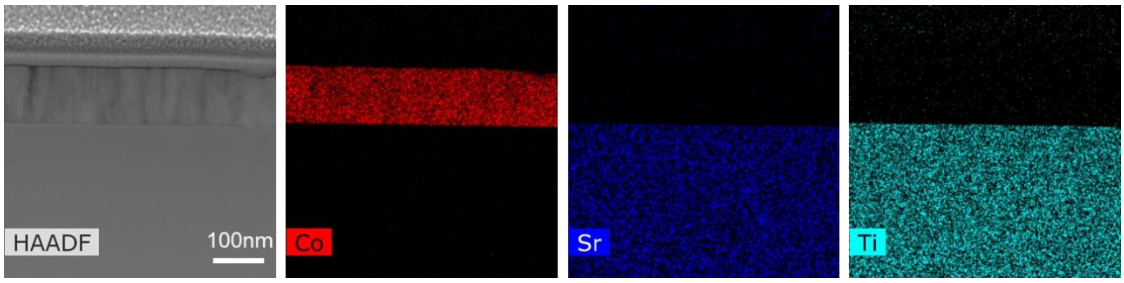


**Fig. S1.** STEM-HAADF image of the pristine LCO film and corresponding STEM-EDS mapping to show the uniform distribution of Co, Sr and Ti in pristine LCO film and STO substrate.

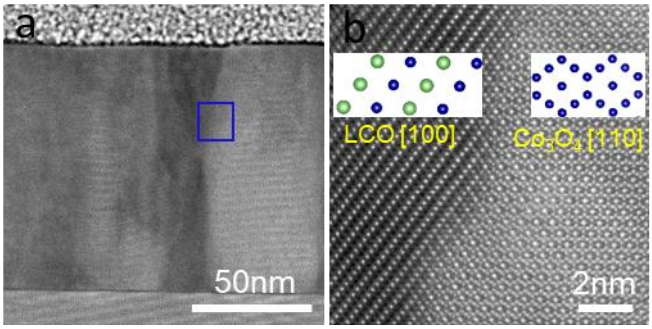


**Fig. S2.** STEM-HAADF images of LCO and $Co_3O_4$ impurity.

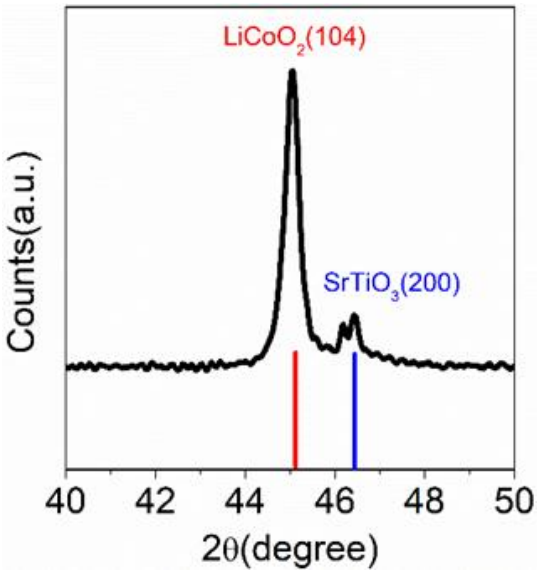


**Fig. S3.** XRD pattern of the pristine LCO epitaxial film.

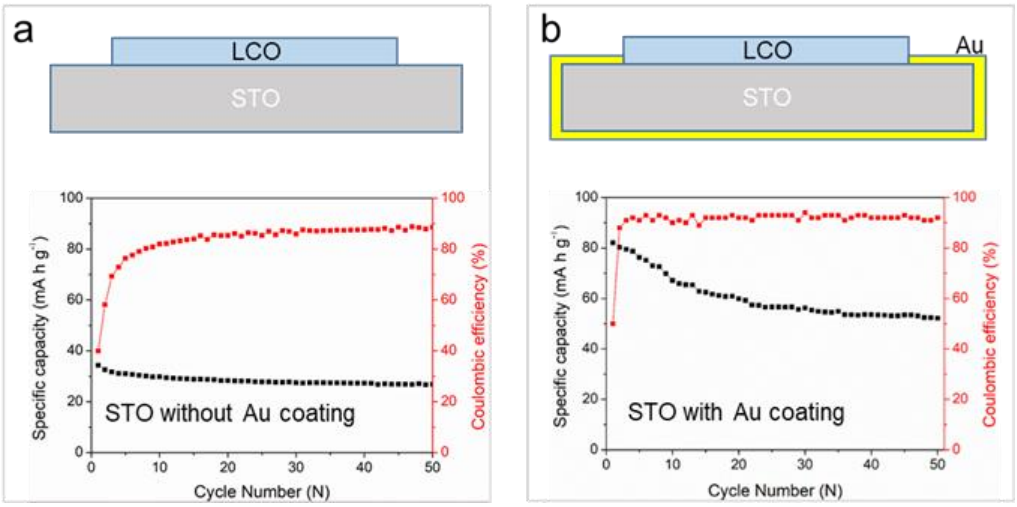


**Fig. S4.** Capacity retentions and corresponding coulombic efficiencies of the LCO film cycled at 0.2C rate (1C=140 mAh g-1) with 2.7 V-4.5 V voltage window, (a) without and (b) with Au coating on STO.

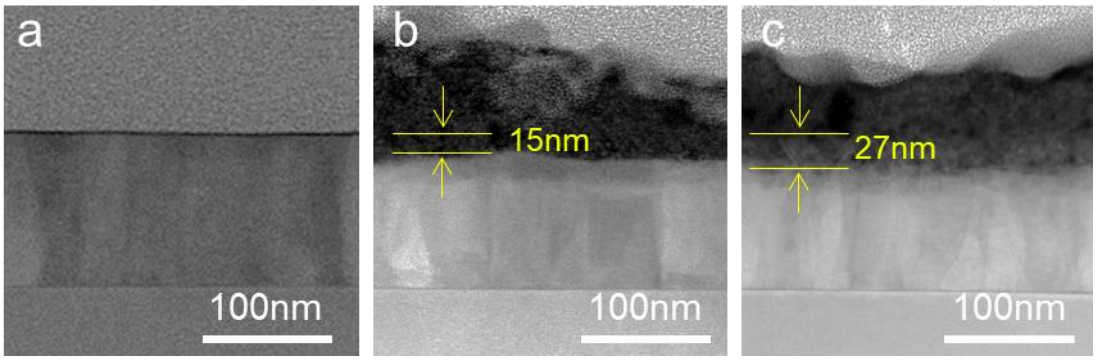


**Fig. S5.** STEM-HAADF images of the pristine LCO film (a) and the film after 50 cycles at 2.7 V-4.5 V (b, c), demonstrating the corrosion layer thickness.

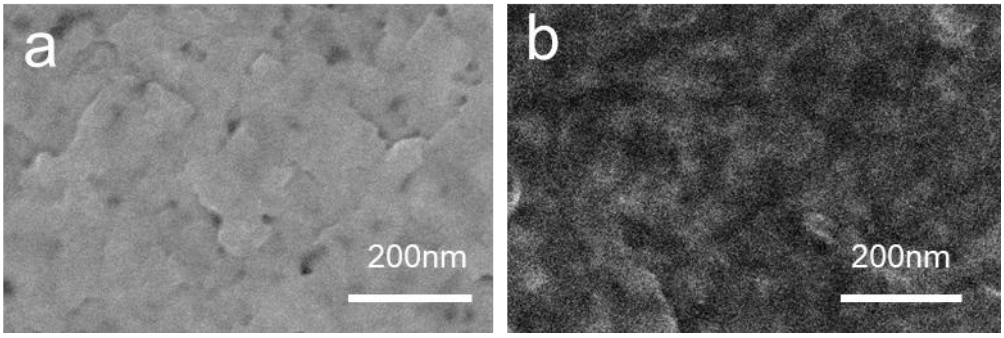


**Fig. S6. (a)** SEM images of the pristine LCO film surface. **(b)** SEM images of the LCO film surface after 50 cycles at 2.7-4.5 V.

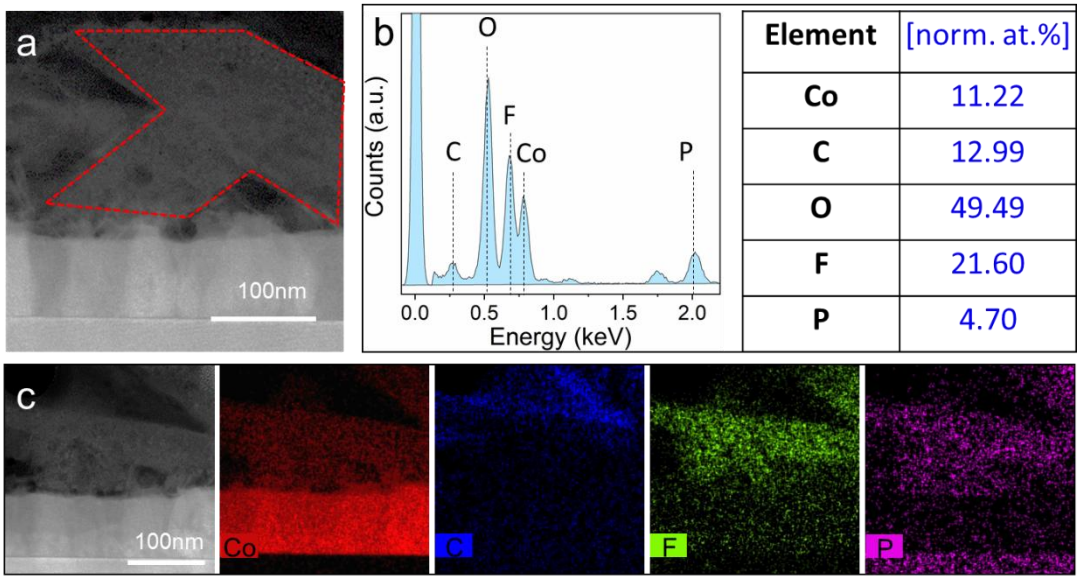


| Element | [norm. at.%] |
|---|---|
| Co | 11.22 |
| C | 12.99 |
| O | 49.49 |
| F | 21.60 |
| P | 4.70 |

**Fig. S7. (a)** A STEM-HAADF image of the LCO film and CEI layer. **(b)** The EDS spectrum and quantification results acquired from the red area in (a). **(c)** EDS mapping of LCO film and CEI layer.

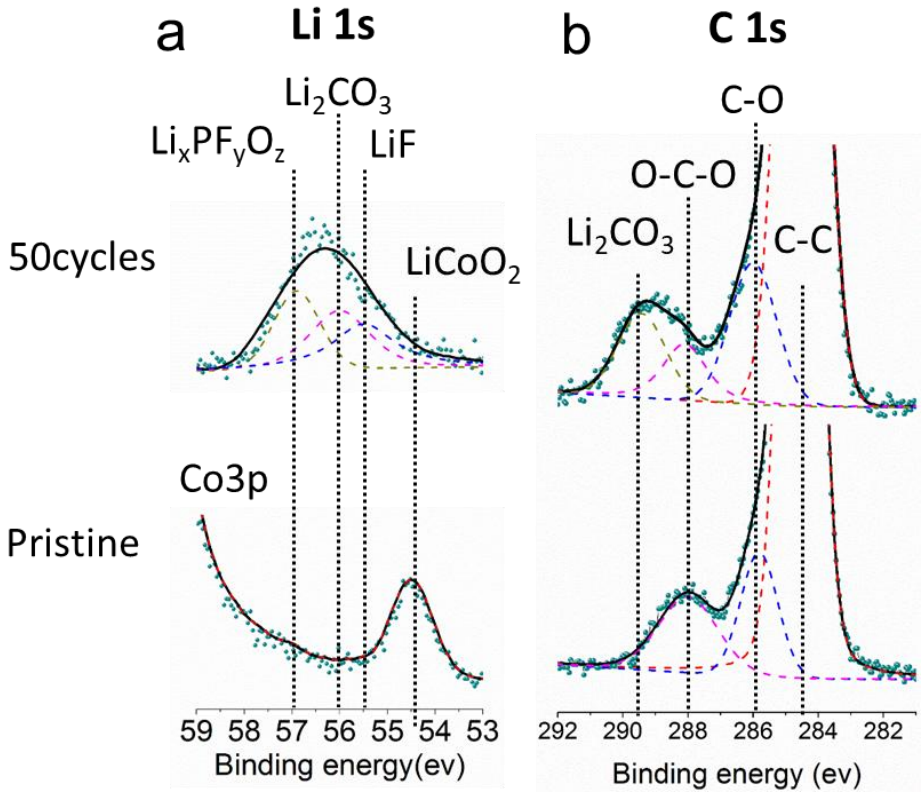


**Fig. S8 (a)** Li1s and **(b)** C1s XPS spectra of the LCO film at pristine state and after 50 cycles at 2.7 V-4.5 V.

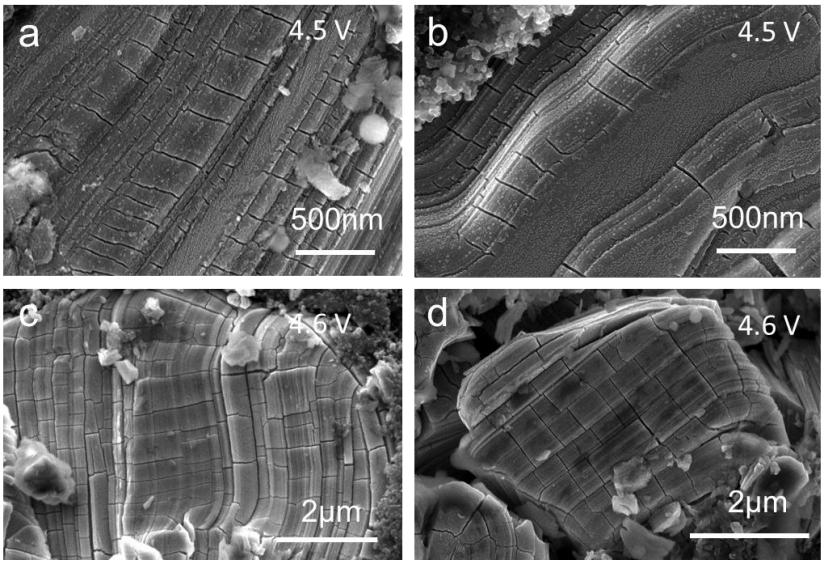


**Fig. S9.** (a, b) SEM images of the LCO particles after 100 cycles at 2.7 V-4.5 V. (c, d) SEM images of the LCO particles after 200 cycles at 2.7 V-4.6 V. High density of surface cracks are observed in both samples.

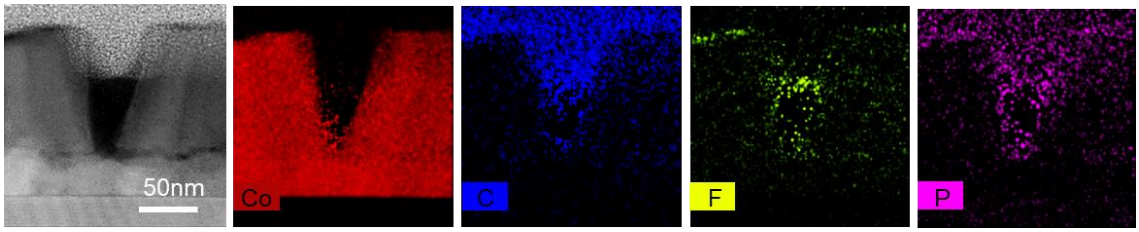


**Fig. S10.** EDS mapping of LCO film at the position with a crack to show that a large amount of carbon, fluorine and phosphorus accumulated inside the crack.